

Hypersonic Flow over a Cylinder with a Nanosecond Pulse Electrical Discharge

Nicholas J. Bisek* and Jonathan Poggie†

U.S. Air Force Research Laboratory, Wright–Patterson Air Force Base, Ohio 45433-7512

and

Munetake Nishihara‡ and Igor Adamovich§

Ohio State University, Columbus, Ohio 43210

DOI: 10.2514/1.T4014

A computational study of Mach 5 airflow over a cylinder with a dielectric barrier discharge actuator was performed. The actuator was pulsed at nanosecond time scales and it rapidly added thermal energy to the flow, creating a shock wave that traveled away from the pulse source. As the shock wave traveled upstream, it interacted with the standing bow shock, and temporarily increased the bow shock standoff distance. This phenomenon was also observed experimentally through phase-locked schlieren photography. This paper aims to reproduce flow phenomena observed in the experiment using high-fidelity computations in order to provide additional insight into the shock–shock interaction, and subsequent effect on the cylinder, through a reduced-order phenomenological model of the actuator. A three-dimensional simulation of the experiment was able to accurately capture the complex cylinder/tunnel-sidewall interaction, and to replicate the changes in the flow produced by the nanosecond dielectric barrier discharge. The results show that the device was very effective at moving the standing bow shock for a minimal energy budget.

I. Introduction

A RECENT experimental study [1] of a nanosecond pulse dielectric barrier discharge (ns-DBD) in a Mach 5 flow demonstrated the feasibility of a plasma-based supersonic flow controller. In the experiment, a bow shock perturbation on a microsecond time scale was detected in phase-locked schlieren visualization [2]. A compression wave was generated, due to rapid localized heating from the DBD, which propagated upstream from the cylinder surface and interacted with the standing bow shock. This interaction temporarily increased the shock standoff distance, with the series of events repeated at an interval of $10\ \mu\text{s}$ (100 kHz).

Previous demonstrations using the ns-DBD have included separated flow reattachment in airflows [3] up to Mach 0.85, characterization of compression wave propagation in a quiescent air [2], and visualization [4] of a large-scale, spanwise vortex over the airfoil at Mach 0.3. The flow control mechanism in these experiments [2–4] appears to be consistent with a localized arc filament plasma actuator (LAFA) [5–7]. This device disrupts the flow with high-amplitude, high-bandwidth perturbations, with a modulation frequency near one of the flow instability frequencies, thereby triggering subsequent growth. Prior flow control studies [5–7] using LAFA actuators in atmospheric pressure jet flows for Mach 0.9 to Mach 2 demonstrated significant localized heating and repetitive shock wave formation by the plasma, large-scale coherent structure generation, and mixing enhancement. These effects were achieved at a low actuator power ($\sim 10\ \text{W}$ per actuator) and by forcing

frequencies near the jet column instability frequency [7]. This low power budget contrasts with previous bow shock control studies, which typically have power budgets on the order of 10 kW using pulsed DC discharges [8], pulsed microwave discharges [9], and laser optical breakdown [10,11].

The present work complements the recent experimental study [1] by replicating the demonstrated effect of the ns-DBD using the fluid dynamics code, LeMANS [12,13]. This was accomplished by imitating the rapid energy coupling of the ns-DBD via phenomenological volumetric energy deposition model [14]. The approach was based on the assumption that the primary flow control mechanism of the ns-DBD is rapid thermal energy release. Many parameters of interest, such as flowfield velocity vectors, surface pressure, and thermal loading, were not available from the experiment. Thus, the computational component of the joint study provided additional details and insight about the baseline flow and the flow perturbation mechanism. In addition, the present work developed a reduced-order model that replicated the effect of the ns-DBD. The reduced-order model can be used in future studies to evaluate the effectiveness of, and optimize the use for, the ns-DBD in practical applications, such as flow control in a hypersonic inlet, isolator, and/or engine exhaust.

II. Experimental Facilities

The experiments were conducted in a small-scale Mach 5 nonequilibrium wind tunnel that was operated using dry air supplied from high-pressure cylinders, at plenum pressures of $p_0 = 49.3\ \text{kPa}$, and a mass flow rate of $7\ \text{g/s}$. The steady-state run time at constant static pressure in the supersonic test section was up to 10 s, which was sufficiently long for the blowdown flow to achieve equilibrium conditions within the inviscid core of the test section and to conduct the ns-DBD experiments. The flow expanded through a nozzle with a design Mach number of 5 and had a throat height of $1.6\ \text{mm}$, as seen in Fig. 1. The top and bottom walls of the supersonic test section continue to diverge after the nozzle exit (at an angle of $1.5\ \text{deg}$), in order to provide boundary layer relief. Rectangular, UV-grade, fused-silica windows were flush mounted on all four walls in the test section to provide optical access for schlieren photography, emission spectroscopy, planar laser-induced fluorescence (PLIF) visualization/thermometry [15,16], molecular tagging velocimetry (MTV) [17,18] diagnostics, and picosecond coherent anti-Stokes Raman scattering measurements [19].

Presented as Paper 2012-186 at the 50th AIAA Aerospace Sciences Meeting including the New Horizons Forum and Aerospace Exposition, Nashville, TN, 9–12 January 2012; received 14 August 2012; revision received 19 August 2013; accepted for publication 21 August 2013; published online 7 January 2014. This material is declared a work of the U.S. Government and is not subject to copyright protection in the United States. Copies of this paper may be made for personal or internal use, on condition that the copier pay the \$10.00 per-copy fee to the Copyright Clearance Center, Inc., 222 Rosewood Drive, Danvers, MA 01923; include the code 1533-6808/14 and \$10.00 in correspondence with the CCC.

*Research Aerospace Engineer, AFRL/RQHF, Senior Member AIAA.

†Research Mechanical Engineer, AFRL/RQHF, Associate Fellow AIAA.

‡Postdoctoral Researcher, Nonequilibrium Thermodynamics Laboratories, Department of Mechanical Engineering, Member AIAA.

§Professor, Nonequilibrium Thermodynamics Laboratories, Department of Mechanical Engineering, Associate Fellow AIAA.

Report Documentation Page			Form Approved OMB No. 0704-0188		
Public reporting burden for the collection of information is estimated to average 1 hour per response, including the time for reviewing instructions, searching existing data sources, gathering and maintaining the data needed, and completing and reviewing the collection of information. Send comments regarding this burden estimate or any other aspect of this collection of information, including suggestions for reducing this burden, to Washington Headquarters Services, Directorate for Information Operations and Reports, 1215 Jefferson Davis Highway, Suite 1204, Arlington VA 22202-4302. Respondents should be aware that notwithstanding any other provision of law, no person shall be subject to a penalty for failing to comply with a collection of information if it does not display a currently valid OMB control number.					
1. REPORT DATE MAR 2014		2. REPORT TYPE		3. DATES COVERED 00-00-2014 to 00-00-2014	
4. TITLE AND SUBTITLE Hypersonic Flow over a Cylinder with a Nanosecond Pulse Electrical Discharge			5a. CONTRACT NUMBER		
			5b. GRANT NUMBER		
			5c. PROGRAM ELEMENT NUMBER		
6. AUTHOR(S)			5d. PROJECT NUMBER		
			5e. TASK NUMBER		
			5f. WORK UNIT NUMBER		
7. PERFORMING ORGANIZATION NAME(S) AND ADDRESS(ES) U.S. Air Force Research Laboratory, AFRL/RQHF, Wright-Patterson AFB, OH, 45433-7512			8. PERFORMING ORGANIZATION REPORT NUMBER		
9. SPONSORING/MONITORING AGENCY NAME(S) AND ADDRESS(ES)			10. SPONSOR/MONITOR'S ACRONYM(S)		
			11. SPONSOR/MONITOR'S REPORT NUMBER(S)		
12. DISTRIBUTION/AVAILABILITY STATEMENT Approved for public release; distribution unlimited					
13. SUPPLEMENTARY NOTES					
14. ABSTRACT					
15. SUBJECT TERMS					
16. SECURITY CLASSIFICATION OF:			17. LIMITATION OF ABSTRACT Same as Report (SAR)	18. NUMBER OF PAGES 9	19a. NAME OF RESPONSIBLE PERSON
a. REPORT unclassified	b. ABSTRACT unclassified	c. THIS PAGE unclassified			

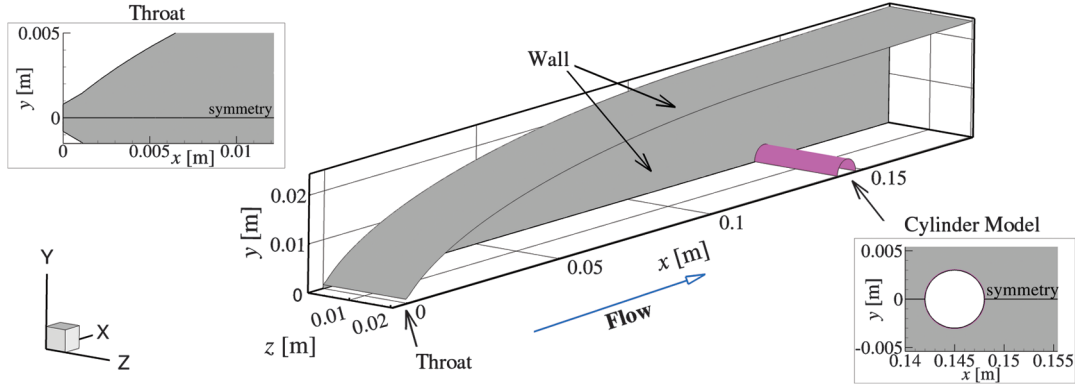


Fig. 1 Computational domain of a Mach 5 nonequilibrium wind tunnel with only one-fourth of the geometry illustrated due to symmetry.

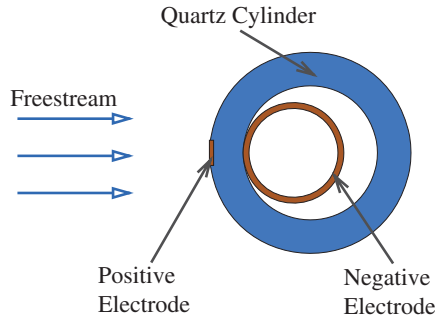


Fig. 2 Cross section of a 6 mm quartz cylinder with the surface and immersed electrodes in the ns-DBD experiment.

A bow shock was generated within the test section by a 6-mm-outer-diam (4-mm-inner-diam) cylinder model composed of quartz, which acted as a dielectric for the ns-DBD actuator. The model was centered 145 mm downstream of the throat (35 mm downstream of the end of nozzle contour), where the tunnel cross section was 40 mm \times 46 mm (width \times height). The model was 40 mm long with its ends affixed to the sidewall windows.

Figure 2 provides a side-view schematic of the electrode configuration for the ns-DBD with the various components proportionally scaled. One actuator electrode was composed of a 10-mm-long, 3-mm-diam copper tube with a wall thickness of 0.35 mm and was immersed inside the quartz tube. Because the interior diameter of the quartz cylinder was 4 mm, the tube electrode was positioned to contact the dielectric near the upstream side of the quartz cylinder so the plasma column induced during the ns-DBD discharge was approximately centered along the stagnation line. The other electrode consisted of a strip of adhesive copper tape 1.5 mm wide by 12 mm long and was affixed to the windward surface of the model. The ends of the exposed copper tape electrode were covered by nonconducting polyimide tape such that the two actuator electrodes overlapped over a spanwise distance of 10 mm, with the surface electrode centered behind the inviscid core bow shock. Output pulse voltage and current were measured during each run. Measured peak voltage and current were 27 kV and 70 A, respectively. Thus, each discharge coupled between 47 mJ/pulse and lasted on the order of 100 ns.

Time evolution of the shock generated by the ns-DBD was captured on phase-locked schlieren images and showed that the discharge pulse generated a compression wave that propagated upstream and locally pushed the steady-state bow shock away from the cylinder. The interaction temporarily increased the bow shock standoff distance by up to 25% [1]. The perturbed region bent away from the flow stagnation line, convected downstream, and eventually the shock envelop returned to its baseline shape about 20 μ s after the discharge event. Image sets from the microsecond-scale shock–shock interaction were collected both for a single-pulse mode (pulse repetition rate of 200 Hz), and double-pulse mode. The later

corresponds with two pulses separated by a 10 μ s delay (pulse repetition rate of 100 kHz). Additional details about the Mach 5 ns-DBD experiment are available in [1].

The test section static pressure, $p_\infty = 160$ Pa (± 7 Pa), was measured using a wall pressure tap located on the tunnel sidewall about 40 mm upstream of the cylinder model. The pressure was assumed to be constant through the sidewall boundary, a valid assumption for a thin laminar boundary layer (no experimental measurements taken thus far have indicated the wall boundary layer is turbulent). The freestream velocity was measured using nitrogen dioxide (NO_2) MTV [17,18]. The freestream temperature was measured using nitric oxide (NO) PLIF thermometry with a resultant temperature of $T_\infty = 50$ to 60 K. These measurements were consistent with a freestream temperature obtained using the isentropic flow relations and the freestream pressure ($T_\infty = 56$ K).

The freestream Mach number inferred from the plenum pressure and freestream static pressure was $M_\infty = 4.6$, whereas a freestream Mach number of $M_\infty = 4.8$ was obtained using the Rayleigh pitot formula and one-dimensional (1-D) normal shock relations. The freestream density was inferred using the ideal gas relation ($p_\infty = \rho_\infty RT_\infty$), with the freestream dry air composed of 78% nitrogen (N_2) and 22% oxygen (O_2) by density. Table 1 lists the nominal freestream conditions and uncertainty bounds for the tunnel's test section.

Figure 3 shows a top-down view of a schlieren image during a typical run (without the discharge). The shock standoff distance was measured to be $\Delta S = 1.2$ mm and had a spanwise length of about 10 mm (25% of the test section width). As seen in the image, the bow shock was uniform across the span in the inviscid core flow.

III. Numerical Methods

Flowfield results were obtained using computational fluid dynamics (CFD) to solve the Navier–Stokes equations. The CFD computations were executed using the Michigan aerothermodynamic Navier–Stokes (LeMANS) code, developed at the University of Michigan [20]. LeMANS is a general two-dimensional (2-D)/axisymmetric/three-dimensional (3-D), parallel, unstructured finite volume CFD code, and has been used previously in numerous studies of hypersonic flows [12–14]. LeMANS may be employed with any of three thermodynamic models: perfect gas, equilibrium, and nonequilibrium thermochemistry. LeMANS employs a two-temperature model to account for thermal nonequilibrium, and a

Table 1 Freestream conditions and uncertainty bounds for Mach 5 airflow around a cylinder

Parameter	Value
u_∞ , m/s	719 ± 6
T_∞ , K	56 ± 5
ρ_∞ , g/m ³	9.9 ± 1.3
p_∞ , Pa	160 ± 6.7
M_∞	4.76 ± 0.25

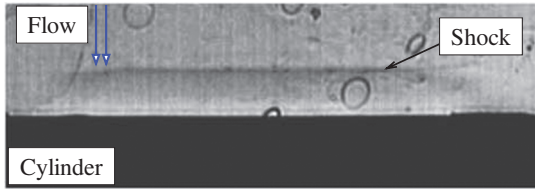


Fig. 3 Schlieren image of the bow shock for Mach 5 airflow over a 6-mm-diam cylinder (top-down view).

standard finite rate chemistry model for nonequilibrium chemistry. Thermal equilibrium was assumed for the present work due to the low freestream temperature and Mach number. LeMANS is primarily used for steady-state simulations, but can compute time-accurate results with first-order temporal accuracy. The simulations were performed using second-order accurate spatial discretization, and carry double precision arithmetic throughout. Spatial and temporal studies conducted in a previous paper [21] indicate that the level of grid resolution and time step used achieved both temporally and spatially independent results.

The ns-DBD controller used in the experiment was, effectively, a thermal actuator, because it produced a flow control mechanism that appeared to be consistent with a LAFPA. However, unlike a LAFPA, where the discharge occurred within a channel embedded in the surface, the DBD's exposed electrode was flush mounted, so it also generated a small body force through the induced ion wind. For the present study, the momentum imparted by the ion wind velocity was assumed negligible in the formation of the compression wave. This assumption may be reevaluated in future work, but it is unlikely that its inclusion into the model will strongly influence the formation of the subsequent compression wave, given that the ion wind would induce a transverse velocity (in contrast to the upstream traveling compression wave). In addition, recent high-fidelity 1-D computations [22] of the ns-DBD showed that the device created a very small region of relatively high ion density and electric field required for the ion wind effect, and that the very high electric field only existed for a short period of time prior to space-charge shielding suppressing the ion wind. As such, acceleration of neutral particles through ion-neutral collisions was very limited, and the majority of the fluid motion was associated with rapid thermal energy transfer into the translational energy mode.

A phenomenological model of dissipative heating was used to represent the ns-DBD actuator. The model was implemented in the Navier–Stokes equations by the addition of a source term, S , to the right side of total energy equation, as shown in Eq. (1). Deposition of all the energy into the translational/rotational mode was a strong assumption, but was adequate for the purpose of this study because it was assumed the compression wave generated by the DBD was due to a rapid transfer of energy into the translation energy mode, as shown in previous work by Popov [23]. The translational energy equation is

$$\frac{\partial E}{\partial t} + \nabla \cdot ((E + p)\mathbf{u} - \boldsymbol{\tau} \cdot \mathbf{u} + \mathbf{q} + \Sigma(\mathbf{J}_{sp}h_{sp})) = S \quad (1)$$

where E is the total energy per volume, p is the pressure, \mathbf{u} is the mass-averaged velocity, $\boldsymbol{\tau}$ is the viscous stress, and \mathbf{q} represents the total heat flux. The species diffusion flux, \mathbf{J}_{sp} , and species enthalpy, h_{sp} , represent energy transport for each species, sp . LeMANS assumed the fluid was continuous, Newtonian, and used Stokes' hypothesis to determine the viscous stresses, which were resolved using Wilke's semi-empirical mixing rule [24].

A close examination of the ICCD images of the plasma from the ns-DBD pulse, taken in front of the cylinder model in Fig. 7 of [1], inferred that the highest concentration of plasma existed just above the cylinder surface and wrapped around the cylinder for approximately 30 deg on either side of the spanwise stagnation line (azimuthal angle $\theta \pm 30$ deg). It was estimated that the plasma layer was 0.05 to 0.12 mm thick, with peak Joule heating assumed to occur about 0.08 mm from the cylinder surface. The image also suggested

that the deposition energy was approximately uniform within the deposition volume, so a hyper-Gaussian distribution function was used to generate a near-uniform deposition rate with the deposition volume, which smoothly and rapidly decayed to zero outside the region. The hyper-Gaussian function was selected because previous work [21] explored a standard Gaussian distribution function and found that it lead to an unrealistically high peak temperature in the flow. The deposition volume was wrapped around the cylinder geometry by expressing the phenomenological ns-DBD model in cylindrical coordinates

$$\begin{aligned} S &= \frac{Q}{Kabc} \exp\left(-\left|\frac{\hat{r}}{a}\right|^\xi - \left|\frac{\hat{\theta}}{b}\right|^\eta - \left|\frac{\hat{z}}{c}\right|^\zeta\right) \\ \hat{r} &= \sqrt{((x - x_{cy})^2 + (y - y_{cy})^2) - r_c} \\ \hat{\theta} &= \tan^{-1} \frac{y - y_{cy}}{x - x_{cy}} \\ \hat{z} &= (z - z_c) \end{aligned} \quad (2)$$

where Q is the total energy deposited and K is a constant such that $\iiint_{-\infty}^{\infty} S r dr d\theta dz = Q$, for the selected values of ξ , η , and ζ . For the wind tunnel geometry shown in Fig. 1, the cylinder was centered at $x_{cy} = 145$ mm, $y_{cy} = 0$, and $z_{cy} = 20$ mm and had a radius of 3 mm. The center of the phenomenological energy deposition volume was 0.1 mm from the cylinder, so $r_c = 3.1$ mm. The deposition volume represented the plasma flow observed in Fig. 7 in [1] by setting $a = 0.04$ mm and $b = 30$ deg. The spanwise extent matched the overlapped electrodes by assigning $c = 5$ mm. Because of its proximity to the cylinder's surface, the power of the radial direction's exponential function was $\xi = 10$, which ensured a nearly uniform deposition rate within the volume and a sharp cutoff outside of it. Some plasma may have existed above the polyimide tape and extended beyond the azimuthal angle of 30 deg, so the radial and spanwise deposition density parameters were set slightly lower: $\eta = 8$, $\zeta = 8$.

IV. 2-D Computations

The top-down schlieren image shown in Fig. 3 highlighted the 2-D structure of the bow shock. A shock-aligned structured mesh was developed for a 2-D computational domain around the 6-mm-diam cylinder, with the stagnation point located at $x = 0.003$ m. A 100×100 mesh was developed for the first 90 deg of the cylinder surface with cell clustering in the radial direction at both the cylinder surface and at the bow shock, whereas azimuthal grid spacing was distributed to ensure orthogonality of the cells at the surface and the shock. A simulation was carried out using the inflow conditions listed in Table 1 and assumed a no-slip, isothermal wall, $T_w = 300$ K. The wall temperature was set to room temperature because of the experiment's short run time and because a previous study [21] explored other boundary conditions (including adiabatic, fully radiative, and partial-slip walls) and found the wall boundary condition did not significantly contribute to the bow shock standoff distance. Temperature contours from the computation were compared with a side-view schlieren image of a bow shock in Fig. 4a.

As seen in the figure, the experiment's bow shock standoff distance, $\Delta S_{exp} = 1.2$ mm, was 20% smaller than the computational standoff distance, $\Delta S_{CFD} = 1.55$ mm. Also displayed in the figure (as a pink line with diamond symbols), is an empirical relation estimating the shock envelope developed by Billig [25] and Ambrosio and Wortman [26], which was in good agreement with the computational shock profile. The discrepancy in the bow shock standoff location suggested there were inappropriate assumptions made in the simulation. An investigation exploring the disparity was performed in previous work [21], which found the uncertainty in freestream conditions accounted for a 3% variation in bow shock location, but no other factors, including rarefaction effects due to partial-slip walls, made an appreciable difference in the bow shock standoff distance. Finally, the two-dimensionality was tested by

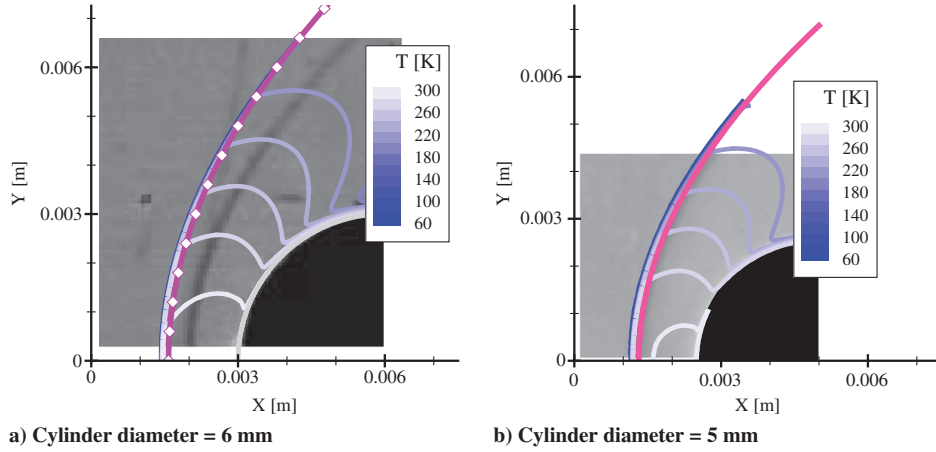


Fig. 4 Contour lines of temperature for Mach 5 airflow over a cylinder. The figures include schlieren images from the experiment and Billig's empirical correlation [25] for the shock envelope (pink line with diamond symbols).

computing flow for a 5-mm-diam cylinder using the same freestream conditions. This scenario was also performed experimentally (although the ns-DBD study has not been carried out on the smaller diameter model). As seen in Fig. 4b, the 5 mm cylinder experimental results were in much better agreement with the computations and Billig's empirical relationship. Thus, the mismatch in shock location for the 6-mm-diam cylinder scenario was attributed to 3-D effects found in the experiment and a calculation of the entire wind tunnel was required.

V. 3-D Computations

A simulation of the entire tunnel (including the nozzle and the region downstream of the test section), was performed to identify the reason for the mismatch in bow shock location observed in the 2-D simulations. Details about the tunnel (including the throat dimensions) were provided in Sec. II, with Fig. 1 outlining of the computational domain used in the simulation. Only one-fourth of the tunnel was simulated because the flow was laminar and the tunnel was symmetric in both the spanwise and transverse directions. The nozzle throat conditions (denoted with a superscript *), are listed in Table 2.

A computational grid was developed for the tunnel using four computational blocks composed of structured cells. The grid spacing was such that grid clustering occurred near all walls, with at least 20 points defining each boundary layer. This level of resolution was sufficient for resolving the laminar, wall-bounded flow, because $\Delta s_w^+ \cong 1$ for all surfaces, where s represents the wall-normal grid spacing along each respective wall, scaled by local inner coordinates (i.e., the friction velocity divided by the kinematic viscosity). A grid resolution study was performed in previous work [21] for the computational block surrounding the cylinder geometry, which also accounted for the unsteady shock interaction due to the ns-DBD pulse. The grid surrounding the cylinder was uniformly spaced in both the x and θ directions to capture the propagation of the ns-DBD's compression wave and subsequent bow shock perturbation. In total, the 3-D computational domain contained about 15 million cells and was run using 512 processors (with a parallel efficiency of $\sim 75\%$). The grid used in the simulation had more than twice the number of

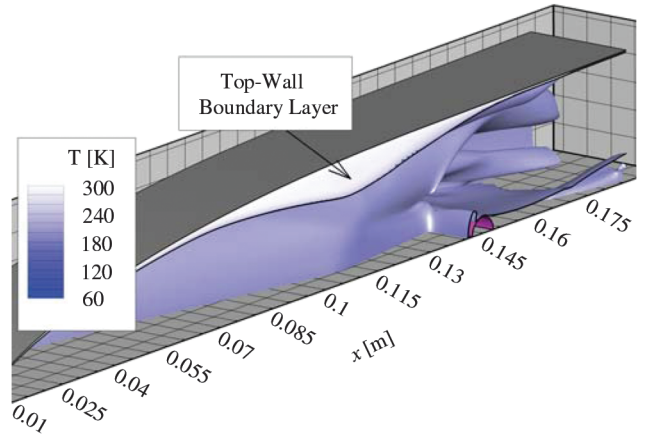


Fig. 5 Mach 1.25 iso-contour colored by temperature at $t = 19$ ms for Mach 5 airflow in the tunnel over a 6-mm-diam cylinder centered 145 mm downstream of the tunnel throat.

cells than a previous simulation of the tunnel performed by Nishihara et al. [16].

No-slip, isothermal walls ($T_w = 300$ K) were assumed for all surfaces and a nonreflective first-order extrapolation was used at the domain exit plane. For the baseline simulation (i.e., without the discharge event), implicit time integration was employed with a time-step size varying from $\Delta t = 0.1$ ns to $\Delta t = 2$ μ s. The simulation was started from quiescent air, with the inflow boundary conditions specified in Table 2. As a result of the quiescent starting conditions, the simulation required ~ 10 ms of simulation time ($\sim 20,000$ computational time steps) for the wall boundary-layer and cylinder bow shock structure to fully develop. The simulation was allowed to evolve for an additional 30 ms of simulation time (30,000 computational time steps at $\Delta t = 2$ μ s), to capture the low frequency oscillation of the sidewall boundary layer/cylinder juncture.

Figure 5 highlights the boundary layer and bow shock structure for the fully developed, quasi-steady solution. As seen in the figure, substantial growth of the sidewall boundary layer was observed upstream of the cylinder model, in contrast to moderate growth of the top-wall boundary layer. The difference was due in part to the 1.5 deg divergence of the top tunnel wall. Figure 5 also shows the midspan planar contour through the top-wall boundary layer that shows the boundary-layer temperature was appreciably higher than in the inviscid core flow due to the isothermal walls and acceleration of the core flow.

Figure 6 shows schlieren images from the experiment that have been overlaid with the computational solutions. The schlieren images were taken with a knife edge set in the streamwise direction. This was replicated from the computational results by plotting contours of the

Table 2 Nozzle throat conditions for the Mach 5 wind tunnel

Parameter	Value
u^* , m/s	318
T^* , K	250
ρ^* , kg/m ³	0.361
p^* , kPa	26
M^*	1.0

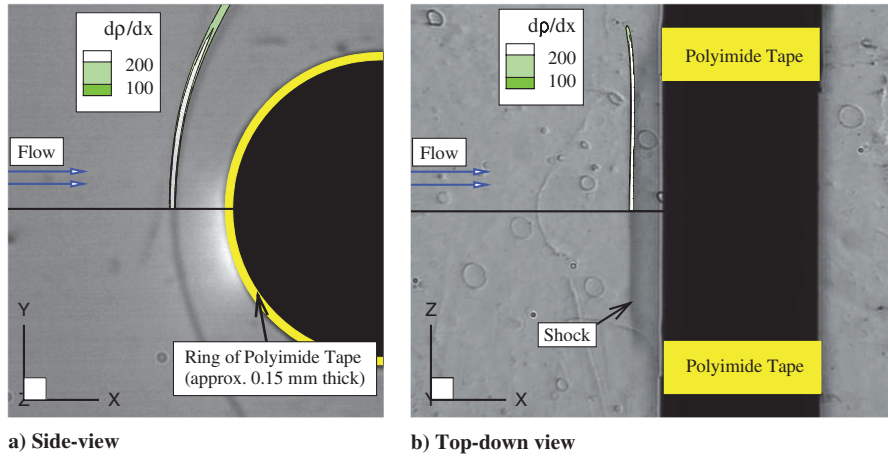


Fig. 6 Schlieren images of Mach 5 airflow over a 6-mm-diam cylinder with the top half of each image overlaid by the computational streamwise density gradient.

streamwise density gradient (with gradients less than 100 kg/m^4 excluded for clarity). The thickness and location of the polyimide tape placed on the cylinder was also identified. As seen in the figure, the computational bow shock location and shock shape are in much better agreement with the experiment, especially compared to the 2-D results presented in Sec. IV.

Aside from schlieren visualization, the only other experimental datum available was a surface pressure measurement located on sidewall of the tunnel, 40 mm upstream of the cylinder. The computed pressure at the location of the pressure tap was $p_w = 147 \text{ Pa}$, which was slightly lower than the experimental value of $p_w = 160 \text{ Pa}$. Given the precision of the experimental measurement ($\pm 7 \text{ Pa}$), and the uncertainties associated with the tunnel conditions, the computational results were considered to be in good agreement with the experiment.

In an ideal wind tunnel, the inviscid flow monotonically accelerates to the desired conditions in the test section. However, the small Mach 5 tunnel used in this work had relatively thick tunnel wall boundary layers. The thick sidewall boundary layer, highlighted in Fig. 5, existed far upstream in the test section. This obstacle caused the inviscid, supersonic, core flow area to shrink and, subsequently, the velocity slowed upstream of the test section ($x \approx 40 \text{ mm}$ upstream of the cylinder). The decreased Mach number coincided with an increase in static pressure within the inviscid core and a higher than anticipated postshock pressure. Figure 7 shows a slice of pressure contours along the transverse symmetry plane. As seen in the figure, there was a large pressure drop in the spanwise direction just after the bow shock. The strong pressure gradient was due to the low pressure in the boundary layer, and was exacerbated by the presence of a necklace vortex that formed within the sidewall boundary layer just upstream of the cylinder.

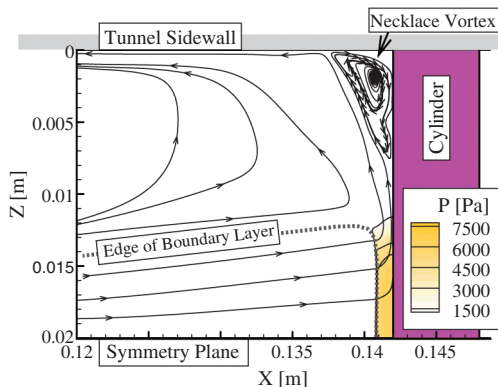


Fig. 7 Top-down view of velocity streamlines and pressure contours for the transverse symmetry plane ($y = 0$) for airflow in a Mach 5 wind tunnel over a 6-mm-diam cylinder.

The large pressure gradient caused a significant portion of the postshock inviscid core flow to turn into the spanwise direction. Although the postshock flow escaping into the boundary layer was subsonic, it had a high velocity, so a large portion of the postshock mass flow was not 2-D. This 3-D effect caused the bow shock location to move much closer to the cylinder than would be expected in a 2-D flow.

The formation of the necklace vortex was the result of a complex interaction between the cylinder and the tunnel sidewall. The vortex experienced a slight oscillation at a fairly low frequency (30 Hz). The low frequency oscillation breathing of the boundary layer is a characteristic of wall/blunt body juncture flows, where a λ shock structure forms at the edge of the inviscid region and the boundary layer [27]. The oscillation occurred in the streamwise direction and produced periodic changes to the cylinder/sidewall wake, which can be seen in Fig. 8. Oscillations at the shock/boundary layer junction were also observed in schlieren images from the experiment. In addition, Fig. 8 shows the existence of a reflected wave that appears downstream of the cylinder wake along the flow spanwise centerline, which impinges on the recirculation zone in the cylinder's wake.

VI. Energy Deposition

With the 3-D simulation results able to replicate the experiment's baseline flow, and able to provide evidence explaining the bow shock location mismatch observed in the 2-D computations, a simulation of the ns-DBD discharge event was carried out. The simulation assumed a total energy deposition $Q = 2 \text{ kW}$ for 50 ns (for one-fourth the geometry), at a time step of $\Delta t = 0.5 \text{ ns}$ to ensure temporal independence based on previous 2-D simulations [21]. Thus, the total energy deposited was 0.4 mJ/pulse , which corresponds to a rapid thermalization of 10% of the input energy. This was qualitatively consistent with kinetic modeling calculations [28], which predicted energy thermalization to occur predominantly within a few tens of nanoseconds after the discharge pulse, with up to $\sim 20\%$ over the first 50 ns. Although Popov [23] suggests the overall thermal efficiency of these types of actuators may be as high as 30%, an efficiency of 10% is a reasonable estimate for the first 50 ns of the discharge.

The simulation was run from the baseline solution for $17 \mu\text{s}$ using a $\Delta t = 0.5 \text{ ns}$ time step (i.e., 34,000 iterations) to capture the evolution of the compression wave/bow shock interaction. Figure 9 shows phase-locked schlieren images at various times after the ns-DBD pulse, along with the computational streamwise density gradient. As seen in the figure, the computations are in excellent agreement with the experiment for the first $6 \mu\text{s}$, which corresponds to the maximum extent of the experiment's perturbed bow shock.

Figure 10 plots distributions of the nondimensional pressure coefficient, $C_p = 2(p - p_\infty)/(\rho_\infty u_\infty^2)$, and nondimensional heat transfer coefficient, $Ch = 2q/(\rho_\infty u_\infty^2)$ along the surface of the cylinder at various times after the ns-DBD pulse. The curves were

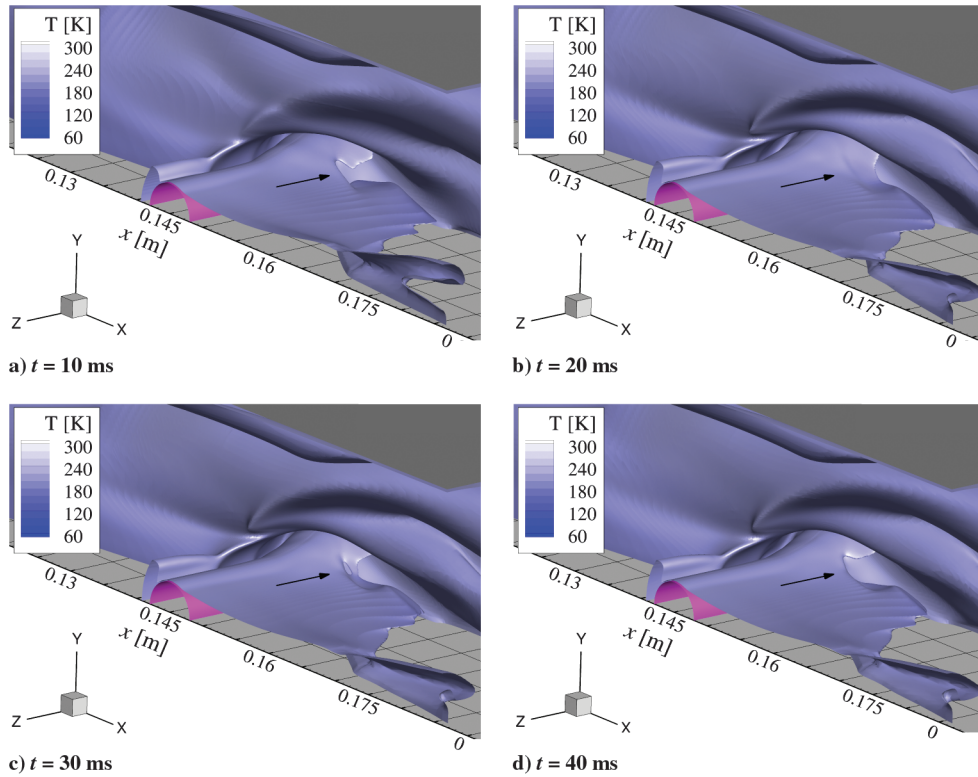


Fig. 8 Mach 1.25 iso-surface colored by temperature for Mach 5 airflow in the tunnel over a 6-mm-diam cylinder, illustrating the breathing of the tunnel sidewall/cylinder wake over a 30 ms cycle (~ 30 Hz).

spanwise-averaged over the region of the cylinder subjected to the inviscid core flow ($0.015 \text{ m} \leq z \leq 0.025 \text{ m}$), because that region corresponds with the spanwise extent of the ns-DBD deposition model and was consistent with the placement of the electrodes in the experiment.

As seen in Fig. 9, the rapid energy deposition of the ns-DBD creates a strong compression wave that moves upstream to interact with the standing bow shock. However, the rapid volumetric deposition, which was centered a small distance away from the cylinder, also created a streamwise moving wave that interacted with the cylinder and, momentarily, but significantly, increased the stagnation region surface pressure ($\theta = 45^\circ$), as seen in Fig. 10a. The elevated surface pressure corresponds with an increase in drag on the cylinder, but the drag augmentation starts to subside as the wave expands around the cylinder. About $4 \mu\text{s}$ after the pulse, the surface pressure fell below the baseline solution, which coincided with a

slight reduction in total drag on the cylinder vs the baseline scenario. Just prior to this event, the upstream-moving compression wave began interacting with the bow shock ($\sim 3 \mu\text{s}$ after the pulse), which caused the bow shock to move away from the cylinder. As a result, the surface pressure continued to drop on the windward side of the cylinder until $\sim 10 \mu\text{s}$ after the pulse, which corresponded with the maximum outward extent of the bow shock in the simulation. As the solution continued to evolve, the surface pressure gradually returned to its original distribution and the bow shock moved back to its original standoff distance.

The nondimensional heat transfer distributions in Fig. 10b show similar behavior, with the rapid energy deposition process raising the local translational temperature and causing a large increase in surface heating. Surface profiles shortly after the ns-DBD pulse show that the peak heating did not occur along the stagnation line, but rather was located about 20° away from the symmetry plane. This was due to

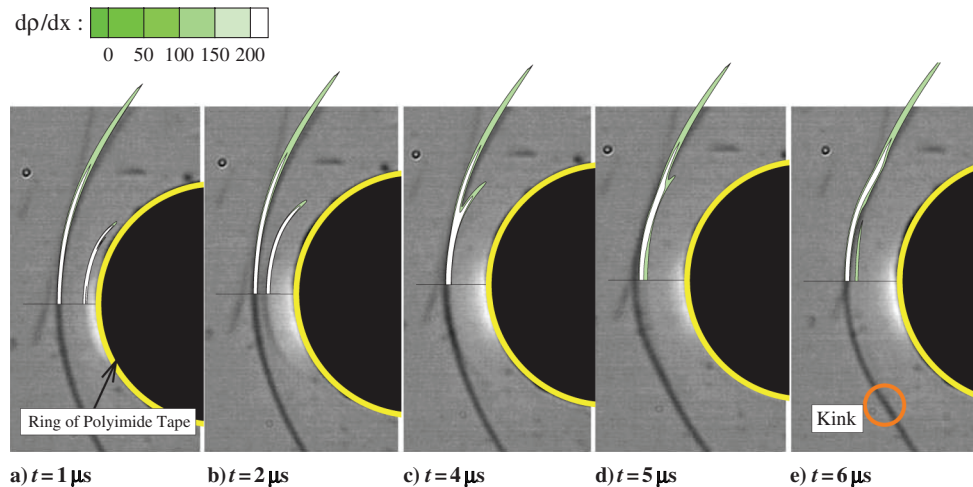


Fig. 9 Side-view schlieren images for Mach 5 airflow over a 6-mm-diam cylinder with the top half of each image overlaid by the computational streamwise density gradient for various time delays after the ns-DBD pulse.

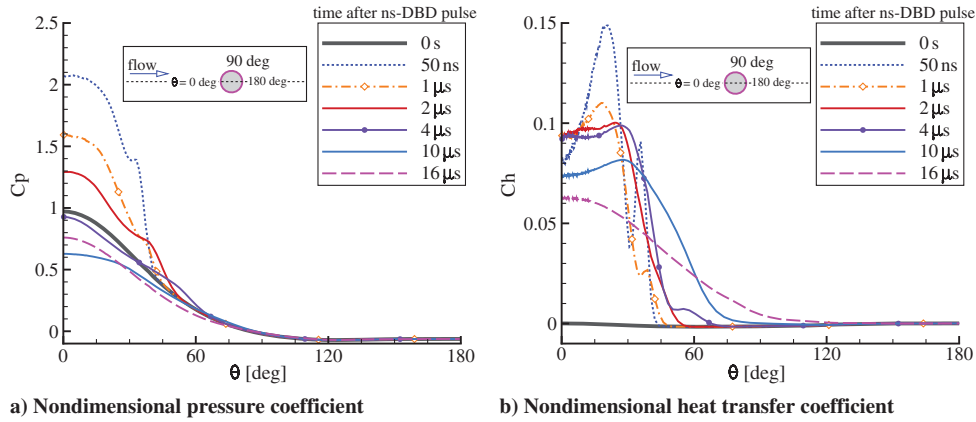


Fig. 10 Spanwise-averaged distributions of nondimensional pressure and heat transfer coefficients along the surface of the cylinder in the inviscid core ($0.015 \text{ m} \leq z \leq 0.025 \text{ m}$).

the uniformity of the energy deposition in the azimuthal direction and that the deposition was centered a small distance from the surface, so the heated flow moved away from the stagnation line as it moved toward the cylinder. Unfortunately, high heat loading on the windward side of the cylinder persisted, even after the initial wave moved past the cylinder and the bow shock/compression wave interaction reached its furthest extent. This occurred because the energy was deposited in the stagnation region of the flow, which required a longer time to dissipate than if it had been placed in the freestream. In addition, radiation in the visible spectrum was observed in the experiment [1], but the fluid code lacked a radiation model to remove energy from the computational domain. Likewise, the imposed isothermal wall boundary condition did not allow for any of the deposition energy to be absorbed by the cylinder.

Figure 10 also shows the aft portion of the cylinder was largely unaffected by the ns-DBD pulse due to the large, very low density recirculation zone established in the cylinder's wake. The extent of the recirculation region was apparent in Fig. 8, which shows the region stretching about 0.24 m (4 cylinder diameters) downstream of the model. Overall, the ns-DBD provided a slight decrease in total drag over the entire ns-DBD cycle, but the improvement was dwarfed by the large increase in peak and total heating experienced by the cylinder.

As previously noted, the computations diverge slightly from the experiment $\sim 6 \mu\text{s}$ after the ns-DBD pulse. Although the computational compression wave speed was similar to that observed in the experiment, its strength was greater. Thus, the perturbed bow shock continued outward for an additional $3 \mu\text{s}$ and, consequently, the perturbed bow shock also took longer to return to its baseline state. These results indicate that in the model, S , the total coupled energy, Q , and/or the duration of the deposition, τ , may need adjustment. In particular, the compression wave appeared overly strong near the stagnation line, which implies that the azimuthal extent of the deposition volume should be increased (i.e., $b > 30$ deg). This hypothesis was based on a close investigation of Fig. 9e, which showed a slight kink in the simulation's perturbed bow shock $\theta \sim 40$ deg from the stagnation line. This kink was also observed and highlighted on the schlieren image, though it occurred ~ 60 deg from the stagnation line. This inconsistency suggests the model volume did not extend far enough around the cylinder and/or the parameter, η , which controlled the deposition decay rate in the radial direction was too large and should be reduced.

Expanding the size the deposition region will weaken the compression wave strength, while not significantly slowing its speed. A weaker wave should allow the perturbed bow shock to return to its nominal location at a rate closer to that observed in the experiment, because the temperatures in the stagnation region would be lower and the perturbed bow shock would not be displaced as far. Likewise, performing an additional simulation of the entire interaction using an adiabatic wall boundary condition, or better, coupling the cylinder surface boundary to a 3-D conjugate heat-transfer model, like the model developed by Amon [29], would allow some of the deposition

energy to be absorbed into the cylinder surface as the solution evolved. This change in the fluid code's run conditions should also allow the perturbed bow shock to relax back to its baseline state more quickly because it would provide an additional avenue for the deposition energy located in the stagnation region to dissipate out of the solution domain. However, the extra computations needed to fine tune the 3-D phenomenological model and cylinder boundary condition are beyond the current resources dedicated for this work.

The results demonstrate the need for developing a nonempirical, physics-based kinetic model of surface ns-DBD to reduce the number of adjustable parameters in the phenomenological model. The physics-based kinetic model needs to predict spatial and time distributions of the energy coupled and thermalized in the ns-DBD actuator, in terms of actuator geometry, voltage pulse shape, temperature, and pressure. Such a model has been developed in [30], but without air plasma kinetics incorporated. Given the high computational cost associated with evaluating the 3-D simulations, it may prove more feasible to experimentally explore the ns-DBD on the smaller 5-mm-diam cylinder because 3-D effects were less pronounced, or to conduct additional repetitions of the existing ns-DBD system for conditions with thinner sidewall boundary layers, so 2-D simulations of the phenomenon can be evaluated.

Although the 3-D computation results did not perfectly replicate the shock behavior observed in the experiment, they did match the experiment quite well for the first $6 \mu\text{s}$ of the ns-DBD pulse. In addition, the solution showed that the compression wave's interaction with the bow shock was directly responsible for the bow shock movement, and not the result of a spanwise portion of the compression wave interacting with the necklace vortex located inside the sidewall boundary layer. Had the latter occurred, the interaction between the compression wave and the necklace vortex would have generated spanwise relief to the flow (i.e., the flow would become more 2-D). As seen in the 2-D analysis of the 5-mm-diam cylinder flow and the discussion in the analysis of the 3-D flow, a more 2-D flow would also experience an increase in the bow shock standoff distance because less of the postshock flow would escape into the sidewall boundary layer. This was not the case, because the compression wave's interaction with the core flow bow shock began $3 \mu\text{s}$ after the start of the ns-DBD discharge, which was much sooner than the compression wave's interaction with the necklace vortex. In addition, the necklace's vortex unsteady influence on the flow occurred on a time scale three orders of magnitude slower than those observed using the ns-DBD actuator. As such, the complex sidewall flow did not have sufficient time to influence the core flow perturbations studied here.

VII. Conclusions

A computational study of Mach 5 airflow around a 6 mm cylinder with a nanosecond DBD discharge was carried out using high-fidelity numerical simulations to explore the impact the discharge had on the flow. The shock standoff distance for the 6 mm cylinder scenario was

found to be 20% smaller in the experiments than the predictions of the empirical correlation and 2-D computations. However, the shock standoff distance for a 5 mm cylinder computation agreed well with the experiment. A 3-D simulation of the entire wind tunnel was subsequently performed, which replicated the bow shock structure seen in schlieren photographs, predicted the width of the tunnel's inviscid core, and matched the measured sidewall static pressure. Having matched the experiment's bow shock location in the 3-D computation, the discrepancy in the bow shock location observed in the 2-D simulations was attributed to the formation of a λ shock structure near the junction of the cylinder and sidewall. As a result, the flow developed a thick sidewall boundary layer upstream of the test section and a strong necklace vortex formed around the cylinder at the sidewall junction. These features resulted in a complex, quasi-steady boundary layer that increased the postshock spanwise velocity, thereby drawing the bow shock closer to the cylinder, even though the experiment's schlieren images and the simulation's streamwise density gradient contours both showed the bow shock structure to have very little spanwise variation within the inviscid core flow test section.

A 3-D simulation of the entire tunnel with the nanosecond pulse was also carried out and was able to match the compression wave speed and the resultant perturbed shock wave speed for the first 6 μ s after the deposition, which corresponded to the peak location of the perturbed bow shock in the experiment. However, the compression wave in the computation was too strong near the stagnation line, which pushed the bow shock outward an additional 20% over the next 3 μ s. Although these results do not agree perfectly with the experiment during the later portion of the discharge cycle, the behavior of the shock perturbation was found to be independent of the form of energy input (due to the short pulse duration), so the resultant flow perturbation was accurately simulated. In addition, the results indicate that the cylinder/sidewall junction was not immediately influenced by the discharge event, so the change in the bow shock standoff distance was a direct result of the nanosecond pulse surface DBD, and not a secondary effect due to the compression wave's interaction with the necklace vortex in the sidewall boundary layer.

The nanosecond DBD actuator produced a strong compression wave, which yielded a minor decrease in total drag to the cylinder over the lifetime of the discharge cycle at the expense of a large increase in peak surface heating. Although the device was not very effective at improving the cylinder's surface conditions, it was very effective at moving a strong standing shock for a very minimal energy budget. As such, this technology could prove very useful in supersonic inlets and isolators found in SCRAM jet engines, where engine un-start continues to be a technical challenge.

Acknowledgments

The authors would like to acknowledge the Department of Defense High Performance Computing Modernization Program, the U.S. Air Force Research Laboratory and the U.S. Army Engineer Research and Development Center for the computation resources needed to conduct this study. The authors would like to thank I. Boyd for allowing the use of his CFD code, LeMANS. This project was sponsored, in part, by the U.S. Air Force Office of Scientific Research under grant number LRIR 12RB09COR (monitored by F. Fahroo, AFOSR/RTA). Work conducted at Ohio State University was funded in part by the Chief Scientist Innovative Research Fund of the U.S. Air Force Research Laboratory Air Vehicles Directorate RB.

References

- [1] Nishihara, M., Takashima, K., Rich, J. W., and Adamovich, I. V., "Mach 5 Bow Shock Control by a Nanosecond Pulse Surface Dielectric Barrier Discharge," *Physics of Fluids*, Vol. 23, No. 6, 2011, Paper 066101. doi:10.1063/1.3599697
- [2] Takashima, K., Zuzeek, Y., Lempert, W. R., and Adamovich, I. V., "Characterization of a Surface Dielectric Barrier Discharge Plasma Sustained by Repetitive Nanosecond Pulses," *Plasma Sources Science and Technology*, Vol. 20, No. 5, 2011, p. 055009. doi:10.1088/0963-0252/20/5/055009
- [3] Roupasov, D. V., Nikipelov, A. A., Nudnova, M. M., and Starikovskii, A. Y., "Flow Separation Control by Plasma Actuator with Nanosecond Pulsed-Periodic Discharge," *AIAA Journal*, Vol. 47, No. 1, 2009, pp. 168–185. doi:10.2514/1.38113
- [4] Little, J., and Samimy, M., "High Lift Airfoil Leading Edge Separation Control with Nanosecond Pulse Driven DBD Plasma Actuators," *AIAA Journal*, Vol. 48, No. 12, 2010, pp. 2884–2898. doi:10.2514/1.J050452
- [5] Samimy, M., Adamovich, I., Webb, B., Kastner, J., Hileman, J., Keshav, S., and Palm, P., "Development and Characterization of Plasma Actuators for High Speed Jet Control," *Experiments in Fluids*, Vol. 37, No. 4, 2004, pp. 577–588. doi:10.1007/s00348-004-0854-7
- [6] Utkin, Y. G., Keshav, S., Kim, J.-H., Kastner, J., Adamovich, I. V., and Samimy, M., "Development and Use of Localized Arc Filament Plasma Actuators for High-Speed Flow Control," *Journal of Physics D*, Vol. 40, No. 3, 2007, pp. 685–695. doi:10.1088/0022-3727/40/3/S06
- [7] Adamovich, I. V., Choi, I., Jiang, N., Kim, J. H., Keshav, S., Lempert, W., Mintusov, E., Nishihara, M., Samimy, M., and Uddi, M., "Plasma Assisted Ignition and High-Speed Flow Control: Non-Thermal and Thermal Effects," *Plasma Sources Science and Technology*, Vol. 18, No. 3, 2009, Paper 034018. doi:10.1088/0963-0252/18/3/034018
- [8] Myrabo, L. N., Raizer, Y. P., Schneider, M. N., and Bracken, R., "Reduction of Drag and Energy Consumption During Energy Release Preceding a Blunt Body in Supersonic Flow," *High Temperature*, Vol. 42, No. 6, 2004, pp. 901–910. doi:10.1007/s10740-005-0035-2
- [9] Lashkov, V., Mashek, I., Anisimov, Y., Ivanov, V., Kolesnichenko, Y., Ryvkin, M., and Gorynya, A., "Gas Dynamic Effect of Microwave Energy Discharge on Supersonic Cone Shaped Bodies," *AIAA Paper* 2004-0671, 2004.
- [10] Adelgren, R. G., Yan, H., Elliott, G. S., Knight, D. D., Beutner, T. J., and Zheltovodov, A. A., "Control of Edney IV Interaction by Pulsed Laser Energy Deposition," *AIAA Journal*, Vol. 43, No. 2, 2005, pp. 256–269. doi:10.2514/1.7036
- [11] Sasoh, A., Sekiya, Y., Sakai, T., Kim, J. H., and Matsuda, A., "Supersonic Drag Reduction with Repetitive Laser Pulses Through a Blunt Body," *AIAA Journal*, Vol. 48, No. 12, 2010, pp. 2811–2817. doi:10.2514/1.J050174
- [12] Scalabrin, L. C., and Boyd, I. D., "Development of an Unstructured Navier–Stokes Solver for Hypersonic Nonequilibrium Aerothermodynamics," *AIAA Paper* 2005-5203, 2005.
- [13] Bisek, N. J., Boyd, I. D., and Poggie, J., "Numerical Study of Magnetoaerodynamic Flow Around a Hemisphere," *Journal of Spacecraft and Rockets*, Vol. 47, No. 5, 2010, pp. 816–827. doi:10.2514/1.49278
- [14] Bisek, N. J., Boyd, I. D., and Poggie, J., "Numerical Study of Plasma-Assisted Aerodynamic Control for Hypersonic Vehicles," *Journal of Spacecraft and Rockets*, Vol. 46, No. 3, 2009, pp. 568–576. doi:10.2514/1.39032
- [15] Nishihara, M., Takashima, K., Jiang, N., Lempert, W., Adamovich, I. V., and Rich, J. W., "Nonequilibrium Flow Characterization in a Mach 5 Wind Tunnel," *AIAA Paper* 2010-4515, 2010.
- [16] Nishihara, M., Takashima, K., Jiang, N., Lempert, W., Adamovich, I. V., Rich, J. W., Doraiswamy, S., and Candler, G. V., "Development of a Mach 5 Nonequilibrium Wind Tunnel," *AIAA Journal*, Vol. 50, No. 10, 2012, pp. 2255–2267. doi:10.2514/1.J051605
- [17] Jiang, N., Webster, M., and Lempert, W. R., "New Advances in Generation of High Repetition Rate Burst Mode Laser Output," *Applied Optics*, Vol. 48, No. 4, 2009, pp. B23–B31. doi:10.1364/AO.48.000B23
- [18] Jiang, N., Nishihara, M., and Lempert, W. R., "Quantitative NO2 Molecular Tagging Velocimetry at 500 kHz Frame Rate," *Applied Physics Letters*, Vol. 97, No. 22, 2010, Paper 221103. doi:10.1063/1.3522654
- [19] Montello, A., Nishihara, M., Rich, J. W., Adamovich, I. V., and Lempert, W., "Picosecond CARS Measurements of Vibrational Distribution Functions in a Nonequilibrium Mach 5 Flow," *AIAA Paper* 2011-1322, 2011.
- [20] Scalabrin, L., "Numerical Simulation of Weakly Ionized Hypersonic Flow Over Reentry Capsules," Ph.D. Dissertation, Dept. of Aerospace Engineering, Univ. of Michigan, 2007.
- [21] Bisek, N. J., Poggie, J., Nishihara, M., and Adamovich, I., "Computational and Experimental Analysis of Mach 5 Air Flow over

- a Cylinder with a Nanosecond Pulse Discharge," AIAA Paper 2012-186, 2012.
- [22] Poggie, J., Bisek, N. J., Adamovich, I., and Nishihara, M., "Numerical Simulation of Nanosecond-Pulse Electrical Discharges," *Plasma Sources Science and Technology*, Vol. 22, No. 1, 2013, Paper 015001.
doi:10.1088/0963-0252/22/1/015001
- [23] Popov, N., "Investigation of the Mechanism for Rapid Heating of Nitrogen and Air in Gas Discharges," *Plasma Physics Reports*, Vol. 27, No. 10, 2001, pp. 886–896.
doi:10.1134/1.1409722
- [24] Wilke, C. R., "A Viscosity Equation for Gas Mixtures," *Journal of Chemical Physics*, Vol. 18, No. 4, 1950, pp. 517–519.
doi:10.1063/1.1747673
- [25] Billig, F. S., "Shock-Wave Shapes around Spherical- and Cylindrical-Nosed Bodies," *Journal of Spacecraft*, Vol. 4, No. 6, 1967, pp. 822–823.
doi:10.2514/3.28969
- [26] Ambrosio, A., and Wortman, A., "Stagnation Point Shock Detachment Distance for Flow Around Spheres and Cylinders," *ARS Journal*, Vol. 33, No. 2, 1962, p. 281.
- [27] Dolling, D. S., "Fifty Years of Shock-Wave/Boundary-Layer Interaction Research: What's Next," *AIAA Journal*, Vol. 39, No. 8, 2001, pp. 1517–1531.
doi:10.2514/2.1476
- [28] Poggie, J., Bisek, N. J., Adamovich, I., and Nishihara, M., "Numerical Simulation of Nanosecond-Pulse Electrical Discharges," AIAA Paper 2012-1025, 2012.
- [29] Amon, C. H., "Spectral Element-Fourier Method for Unsteady Conjugate Heat Transfer in Complex Geometry Flows," *Journal of Thermophysics and Heat Transfer*, Vol. 9, No. 2, 1995, pp. 247–253.
doi:10.2514/3.653
- [30] Takashima, K., Yin, Z., and Adamovich, I. V., "Measurements and Kinetic Modeling Analysis of Energy Coupling Nanosecond Pulse Dielectric Barrier Discharges," AIAA Paper 2012-3039, 2012.